Planar Hall effect sensor bridge geometries optimized for magnetic bead detection

Østerberg, Frederik Westergaard; Rizzi, Giovanni; Henriksen, Anders Dahl; Hansen, Mikkel Fougt

Published in:
Journal of Applied Physics

Link to article, DOI:
10.1063/1.4876256

Publication date:
2014

Document Version
Publisher's PDF, also known as Version of record

AIP | Journal of Applied Physics

Planar Hall effect bridge geometries optimized for magnetic bead detection

Frederik Westergaard Østerberg, Giovanni Rizzi, Anders Dahl Henriksen, and Mikkel Fougt Hansen

Citation: Journal of Applied Physics **115**, 184505 (2014); doi: 10.1063/1.4876256
View online: http://dx.doi.org/10.1063/1.4876256
View Table of Contents: http://scitation.aip.org/content/aip/journal/jap/115/18?ver=pdfcov
Published by the AIP Publishing

Planar Hall effect bridge geometries optimized for magnetic bead detection

Frederik Westergaard Østerberg,[a] Giovanni Rizzi, Anders Dahl Henriksen, and Mikkel Fougt Hansen[b]
Department of Micro- and Nanotechnology, Technical University of Denmark, DTU Nanotech, Building 345 East, DK-2800 Kongens Lyngby, Denmark

(Received 30 January 2014; accepted 1 May 2014; published online 14 May 2014)

Novel designs of planar Hall effect bridge sensors optimized for magnetic bead detection are presented and characterized. By constructing the sensor geometries appropriately, the sensors can be tailored to be sensitive to an external magnetic field, the magnetic field due to beads being magnetized by the sensor self-field or a combination thereof. The sensors can be made nominally insensitive to small external magnetic fields, while being maximally sensitive to magnetic beads, magnetized by the sensor self-field. Thus, the sensor designs can be tailored towards specific applications with minimal influence of external variables. Three different sensor designs are analyzed theoretically. To experimentally validate the theoretical signals, two sets of measurements are performed. First, the sensor signals are characterized as function of an externally applied magnetic field. Then, measurements of the dynamic magnetic response of suspensions of magnetic beads with a nominal diameter of 80 nm are performed. Furthermore, a method to amplify the signal by appropriate combinations of multiple sensor segments is demonstrated. © *2014 AIP Publishing LLC*. [http://dx.doi.org/10.1063/1.4876256]

I. INTRODUCTION

Magnetic beads are considered an important part of the readout and sample manipulation in future biosensors due to the low magnetic susceptibility of biological samples.[1–4] For example, using magnetic beads as readout labels result in almost no magnetic background signal from the biological sample. Moreover, a biosensor based on magnetic detection of magnetic beads may provide a highly sensitive readout in a compact format.

The use of magnetic beads as readout labels in biosensors is traditionally either surface- or volume-based. For surface-based detection, the sensor surface and the magnetic beads are functionalized such that the presence of target analyte results in attachment of beads to the sensor surface. Thus, the target analyte results in an increased concentration of magnetic beads near the sensor surface.[2,5–7] For the volume-based approach, only the beads are functionalized such that the target analyte attaches to the beads. Thus, the presence of the target analyte leads to an increase in the hydrodynamic size of the magnetic beads either due to the size of the target analyte or because the target analyte induces agglutination of beads. The hydrodynamic diameter of the magnetic beads can be determined by measuring the Brownian relaxation frequency.[8]

For both surface- and volume-based sensing, the magnetic beads are traditionally detected by either superconducting quantum interference devices (SQUIDs),[9] inductive methods,[10] fluxgates,[11] magneto-optical methods,[12] or magnetoresistive sensors.[7,13–15] All methods, except for magneto-optical detection, directly measure the magnetic field from the magnetic beads. This implies that these methods will also to some extent be affected by external magnetic fields. Lock-in techniques and various frequency mixing techniques[16–18] are often used to filter away the signal not due to the magnetic beads. However, it is still desired to minimize the signal due to externally applied magnetic fields.

In our previous work, we have shown that magnetoresistive sensors, termed as planar Hall effect bridge (PHEB) sensors, are sensitive to both external fields[19] and to the magnetic field from magnetic beads being magnetized by the magnetic field due to the sensor bias current (the sensor self-field).[15] Here, we systematically analyze and demonstrate how the sensor geometry can be tailored such that the sensor becomes sensitive to only external magnetic fields, only the magnetic field from beads magnetized by the sensor self-field or a combination thereof. Two new designs of planar Hall effect bridge sensors are presented. The first design is nominally insensitive to external magnetic fields, while being maximally sensitive to magnetic beads magnetized by the sensor self-field. The second design is a differential design, which is sensitive to the difference in magnetic fields between the top and bottom of the sensor. This enables analyte detection with an on-chip subtraction of the background signal due to unspecific bound beads and temperature effects. The sensitivities of the sensor designs to magnetic fields and to magnetic beads are derived theoretically and studied experimentally. Consequences for the use of the sensors for magnetic biodetection are discussed.

II. THEORY

A. Sensor construction elements

The sensor designs, in this study, are all built from the same construction element, which is a bar of a magnetoresistive material with length l, width w, and thickness t as shown

[a]Electronic mail: Frederik.Osterberg@nanotech.dtu.dk
[b]Electronic mail: Mikkel.Hansen@nanotech.dtu.dk

in Fig. 1(a). The angle of the magnetization **M** to the x-axis is denoted θ and the angle of the current $\mathbf{I}_{\text{bar}}$ through a bar to the x-axis is denoted α. The resistance of such a magnetoresistive bar is given by[19]

$$R(\alpha,\theta) = \frac{l}{wt}\left[\frac{\rho_{\parallel}+\rho_{\perp}}{2} + \frac{\Delta\rho}{2}\sin(2\alpha)\sin(2\theta)\right], \quad (1)$$

where $\rho_{\parallel}$ and $\rho_{\perp}$ are the resistivities when the current and magnetization are parallel and orthogonal, respectively, and $\Delta\rho = \rho_{\parallel} - \rho_{\perp}$. For a magnetoresistive material exchange-biased along the x-direction, the angle of the magnetization is linear for small magnetic fields H_y applied in the y-direction[19]

$$\theta \approx \frac{H_y}{H_{\text{K}} + H_{\text{ex}}}, \quad (2)$$

where H_{K} and H_{ex} are the anisotropy and exchange fields, respectively. This linear assumption will be used in the further treatment below.

The resistance of a bar can then be written as

$$R(\alpha) = R_0 - \sin(2\alpha)S_0H_y, \quad (3)$$

where R_0 is the resistance of the bar in zero applied magnetic field,

$$R_0 = \frac{l}{wt}\frac{\rho_{\parallel}+\rho_{\perp}}{2}, \quad (4)$$

and S_0 is the low-field sensitivity given by

$$S_0 = -\frac{l}{wt}\frac{\Delta\rho}{H_{\text{ex}}+H_{\text{K}}}. \quad (5)$$

With these assumptions, $R(\alpha)$ depends linearly on H_y.

Let us now consider the contributions to H_y due to an applied external magnetic field, the sensor self-field and magnetic beads being magnetized by these fields. For simplicity, the magnetization of the beads is assumed to be proportional to the magnetic field, such that their susceptibility χ does not depend on the magnitude of the magnetic field. Note that this excludes non-linear magnetization effects from the treatment below. Moreover, to further simplify the treatment, we will only consider a DC external magnetic field applied in the y-direction H_y^{app}. These effects have been central for the use of frequency mixing detection schemes[16–18] that are, hence, not considered in the present work. We generally allow the magnetic bead susceptibility to be complex such that $\chi = \chi' - i\chi''$, where χ' and χ'' are the in-phase and out-of-phase magnetic susceptibilities, respectively.

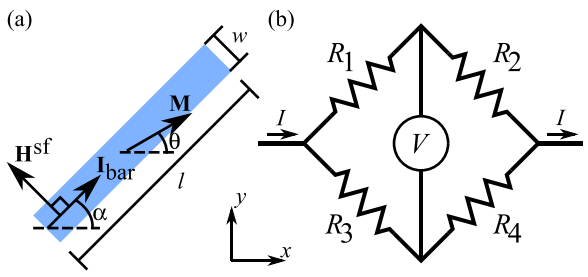

FIG. 1. (a) Bar of a magnetoresistive material used for construction of PHEB sensors. Along with definition of length l, width w, directions of the current, and magnetization of α and θ, respectively. The sketch also shows that the self-field $\mathbf{H}^{\text{sf}}$ will act on the sensor in an angle of $\alpha + \pi/2$. (b) Wheatstone bridge with definition of the four resistors R and the current I inlet and outlet as well as where the bridge voltage V is measured.

The magnetic field acting on the bar in the y-direction, H_y, can be written as

$$H_y = H_y^{\text{ext}} + H_y^{\text{sf}}, \quad (6)$$

where H_y^{ext} is the y-component of the *total* magnetic field experienced by the magnetic field sensor due to an applied external magnetic field and H_y^{sf} is the y-component of the *total* magnetic field experienced by the magnetic field sensor due to the sensor self-field. Both of these contributions may include signals from magnetic beads.

Let us first consider H_y^{ext}. In addition to the applied magnetic field H_y^{app}, the presence of magnetic beads in the applied magnetic field may produce an additional magnetic field that we write as $H_y^{\text{app}}\beta\chi_0$, where χ_0 is the DC magnetic bead susceptibility. Here, β is a dimensionless constant accounting for the effect of averaging the magnetic fields from the beads magnetized by the applied field over the sensor geometry. Thus, we can write

$$H_y^{\text{ext}} = H_y^{\text{app}}(1+\beta\chi_0). \quad (7)$$

Next, we consider the magnetic field due to the sensor self-field. One contribution to this field is from the sensor self-biasing due to current shunted through other layers than the active sensor layer. This contribution depends on the sensor stack and width and its magnitude can be written as $\gamma_0 I_{\text{bar}}$.[20] A second contribution is from magnetic beads being magnetized by the sensor self-field. These give rise to a magnetic field of magnitude $\gamma_1\chi I_{\text{bar}}$, where γ_1 is a positive constant depending on the distribution and amount of magnetic beads as well as the sensor geometry, which relates the current times the magnetic bead susceptibility to the average magnetic field experienced by the sensor due to the magnetic beads.[20,21] In both cases, the direction of the self-field is given by $\hat{\mathbf{H}}_{\text{sf}} = -\hat{\mathbf{I}} \times \hat{\mathbf{z}}$, where $\hat{\mathbf{I}}$ and $\hat{\mathbf{z}}$ are unit vectors along the current direction in the bar and the z-direction, respectively (cf. Fig. 1). The magnitude of the total self-field is given by

$$H^{\text{sf}} = I_{\text{bar}}(\gamma_0 + \gamma_1\chi), \quad (8)$$

and the y-component of the self-field is found by multiplying H^{sf} with $\cos(\alpha)$. Combining the above expressions, Eq. (3) can be written as

$$R(\alpha) = R_0 - \sin(2\alpha)S_0\left[H_y^{\text{ext}} + H^{\text{sf}}\cos(\alpha)\right]. \quad (9)$$

The magnitude of $\sin(2\alpha)$ is maximized for $\alpha = \pi/4 + p\pi/2$ with $p \in \mathbb{Z}$ and we therefore restrict our considerations to these values of α. Inserting in Eq. (9) results in the following set of resistances:

$$R\left(\frac{\pi}{4}\right) = R_0 - S_0 H_y^{\text{ext}} - \frac{1}{\sqrt{2}} S_0 H^{\text{sf}}, \tag{10a}$$

$$R\left(\frac{3\pi}{4}\right) = R\left(-\frac{5\pi}{4}\right) = R_0 + S_0 H_y^{\text{ext}} - \frac{1}{\sqrt{2}} S_0 H^{\text{sf}}, \tag{10b}$$

$$R\left(\frac{5\pi}{4}\right) = R\left(-\frac{3\pi}{4}\right) = R_0 - S_0 H_y^{\text{ext}} + \frac{1}{\sqrt{2}} S_0 H^{\text{sf}}, \tag{10c}$$

$$R\left(\frac{7\pi}{4}\right) = R\left(-\frac{\pi}{4}\right) = R_0 + S_0 H_y^{\text{ext}} + \frac{1}{\sqrt{2}} S_0 H^{\text{sf}}. \tag{10d}$$

These expressions show that the signs of the two terms due to the external field or the self-field can be chosen independently by appropriate choices of angles. Moreover, they can be used to easily identify the values of α that should be used to achieve a given sign combination of the two contributions. Note that changing α by π changes the sign of the self-field contribution, but leaves the term due to the external field unchanged and changing α by $\pi/2$ changes the sign of the external field contribution.

B. Wheatstone bridge signal

The construction elements are arranged in a Wheatstone bridge as shown in Fig. 1(b), where a current I is passed through the sensor in the x-direction and the bridge voltage V is measured across the y-direction. The bridge voltage is generally given by

$$V = I \frac{R_2 R_3 - R_1 R_4}{R_1 + R_2 + R_3 + R_4}. \tag{11}$$

When $R_1 + R_2 = R_3 + R_4$, the current in each branch of the sensor bridge is $I_{\text{bar}} = I/2$ and

$$V = \frac{1}{2} I (R_3 - R_1). \tag{12}$$

This expression is approximately correct, when $R_1 + R_2 \simeq R_3 + R_4$. The resistance of each sensor branch in more complex sensor geometries can be found by adding the contributions from all segments constituting the branch using the above expressions, while paying attention to the direction of the current.

C. Sensor designs

The sensor construction elements can be combined in numerous ways to maximize the sensitivity to the desired input, while minimizing the sensitivity to other inputs. The top part of Fig. 2 shows the three basic designs of the PHEB, parallel PHEB (pPHEB), and differential PHEB (dPHEB) sensors considered in this work, where each sensor branch consists of a single resistor bar ($N = 1$). The bottom part shows the same three sensors for $N = 2$. For all designs, the current is passed through the sensor in the x-direction and the bridge output voltage is measured along the y-direction.

1. PHEB design

The PHEB design was introduced by Henriksen *et al.*[19] They also introduced designs with branches composed of parallel meandering magnetoresistive segments, where the value of α changed by π from one segment to the next. They showed that the signal due to an external magnetic field was proportional to the number of magnetoresistive segments in agreement with the predictions of Eq. (12) using that the external field contributes with the same sign for $R(\alpha)$ and $R(\alpha + \pi)$. The PHEB design with $N = 1$ has also been demonstrated on measurements on magnetic bead suspensions using the sensor self-field as excitation.[22] Our above analysis

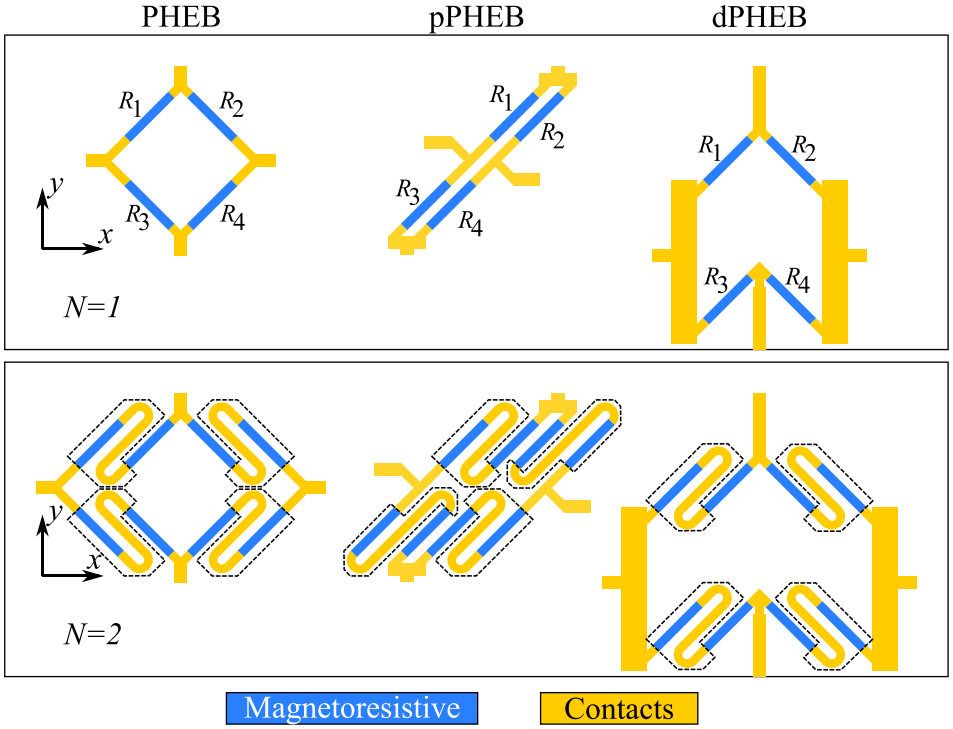

FIG. 2. Sketch of the three different sensor types PHEB, pPHEB, and dPHEB with $N = 1$ and $N = 2$. The magnetoresistive sensor stack is indicated by blue and the contact layer is indicated by yellow. The dashed lines mark the "cells" containing the segments to go from $N = 1$ to $N = 2$. These cells are repeated as needed to obtain general designs with $N > 2$.

shows that for parallel meandering magnetoresistive elements with current directions alternating by π going from one segment to the next, the contributions to the self-field signal from the segments will have alternating signs and thus partially cancel out. To avoid this effect, a new multiple segment PHEB design is presented, where only segments with the same current orientation are made from the magnetoresistive layer, while the other elements are made from the contact layer. From the sketch of the PHEB sensors shown in Fig. 2, it is seen that branches 1 and 4 have $\alpha = \pi/4$ and branches 2 and 3 have $\alpha = -\pi/4$. By assumption, all four branches experience the same external field and self-field. The expected signal is calculated from Eq. (12) and using Eqs. (7) and (8), we obtain

$$V_{\mathrm{PHEB}} = NS_0 I\left[H_y^{\mathrm{ext}} + \frac{1}{\sqrt{2}}H^{\mathrm{sf}}\right], \\ = NS_0\left[H_y^{\mathrm{app}}(1+\beta\chi_0)I + \frac{1}{2\sqrt{2}}(\gamma_0+\gamma_1\chi)I^2\right]. \quad (13)$$

It is seen that the theoretical signal for this PHEB sensor design depends on the external field (including possible contributions from magnetic beads) as well as the self-field both due to self-biasing (γ_0) and to magnetic beads (γ_1).

2. pPHEB design

Moreover, we introduce a design shaped like a parallelogram, the pPHEB, which is designed such that the self-field signals from all sensor branches are additive, whereas the contributions due to the external magnetic field cancel out. For the pPHEB sensors, the angle of the current is $\alpha = \pi/4$ for branches 1 and 4 and $\alpha = 5\pi/4$ for branches 2 and 3. As for the PHEB sensor, all four branches experience the same external field and self-field. From Eq. (12) and using Eq. (8), we obtain

$$V_{\mathrm{pPHEB}} = NS_0 I\frac{1}{\sqrt{2}}H^{\mathrm{sf}}, \\ = NS_0\frac{1}{2\sqrt{2}}(\gamma_0+\gamma_1\chi)I^2. \quad (14)$$

This shows that the signal of the pPHEB sensors nominally only depends on the sensor self-biasing (γ_0) and the signal due to magnetic beads magnetized by the sensor self-field (γ_1). Thus, the signal due to a homogeneous external magnetic field is eliminated.

3. dPHEB design

Finally, we study a differential design, dPHEB, which is designed to eliminate sensor signals from an applied external magnetic field, as well as the sensor self-biasing. For the dPHEB sensor, the angle of the current is $\alpha = \pi/4$ for branches 1 and 3 and $\alpha = -\pi/4$ for branches 2 and 4. All four branches are assumed to be influenced by the same applied magnetic field. However, for this design, we allow the two top branches (1 and 2) to experience a different amount of beads than the bottom two branches (3 and 4). Insertion into Eq. (12) and using Eqs. (7) and (8) gives

$$V_{\mathrm{dPHEB}} = NS_0 I\left[\frac{1}{2}\Delta H_y^{\mathrm{ext}} + \frac{1}{2\sqrt{2}}\Delta H^{\mathrm{sf}}\right], \\ = NS_0\left[\frac{1}{2}\Delta\beta\chi_0 H_y^{\mathrm{app}} I + \frac{1}{4\sqrt{2}}\Delta\gamma_1\chi I^2\right], \quad (15)$$

where Δ denotes the difference between the top and bottom branches, such that $\Delta\beta = \beta_{\mathrm{top}} - \beta_{\mathrm{bottom}}$ and $\Delta\gamma_1 = \gamma_{1,\mathrm{top}} - \gamma_{1,\mathrm{bottom}}$. Thus, in a homogeneous applied magnetic field, the differences between the values of β as well as γ_1 for the top and bottom parts of the sensor bridge are measured. Note that this configuration also eliminates the offset due to self-biasing (γ_0). This design with $N = 1$ was recently introduced by Rizzi *et al.*,[21] who also demonstrated its use for surface-based DNA detection. Here, we introduce designs with $N > 1$ and, moreover, characterize the ability of the design to reject external magnetic fields and the sensor self-biasing.

D. Lock-in detection

The sensor signals are measured using lock-in technique by passing an alternating current $I = I_{\mathrm{AC}}\sin(\omega t)$ of amplitude I_{AC} and frequency $f = \omega/(2\pi)$ through the sensors. The nominal in-phase and out-of-phase components of the n^{th} harmonic signal $V_n = V_n' + \mathrm{i}V_n''$ can be calculated as

$$V_n' = \frac{\sqrt{2}}{2\pi}\int_0^{2\pi}\sin(n\omega t)V(t)\mathrm{d}(\omega t), \quad (16)$$

$$V_n'' = \frac{\sqrt{2}}{2\pi}\int_0^{2\pi}\sin\left(n\omega t + \frac{\pi}{2}\right)V(t)\mathrm{d}(\omega t). \quad (17)$$

The generally complex magnetic susceptibility implies that the magnetic bead response may lag behind the magnetic field excitation. Writing the complex susceptibility in terms of the phase lag ϕ as $\chi = \chi' - \mathrm{i}\chi'' = |\chi|(\cos\phi - \mathrm{i}\sin\phi)$ and including the phase lag in the time-dependent magnetic response from the magnetic beads, the complex sensor output can be obtained. Table I summarizes the nominal in-phase and out-of-phase 1st and 2nd harmonic signals for the three sensor designs calculated by inserting the sensor signals in Eqs. (16) and (17). Note that the in-phase 2nd harmonic sensor signal V_2' is proportional to the out-of-phase magnetic susceptibility χ'' and that the out-of-phase 2nd harmonic sensor signal V_2'' is linearly related to the in-phase magnetic susceptibility χ' for the PHEB and pPHEB designs and proportional to χ' for the dPHEB design.

TABLE I. 1st and 2nd harmonic in-phase and out-of-phase signals calculated for the three sensors designs. The table should be read horizontally such that the prefactor has to be multiplied with each of the sensor signals in each row.

Prefactor	PHEB	pPHEB	dPHEB
$V_1' = \frac{1}{\sqrt{2}}NS_0 I_{\mathrm{AC}}$	$H_y^{\mathrm{app}}(1+\beta\chi_0)$	0	$\frac{1}{2}\Delta\beta H_y^{\mathrm{app}}\chi_0$
$V_1'' = \frac{1}{\sqrt{2}}NS_0 I_{\mathrm{AC}}$	0	0	0
$V_2' = -\frac{1}{8}NS_0 I_{\mathrm{AC}}^2$	$\gamma_1\chi''$	$\gamma_1\chi''$	$\frac{1}{2}\Delta\gamma_1\chi''$
$V_2'' = -\frac{1}{8}NS_0 I_{\mathrm{AC}}^2$	$\gamma_0 + \gamma_1\chi'$	$\gamma_0 + \gamma_1\chi'$	$\frac{1}{2}\Delta\gamma_1\chi'$

III. EXPERIMENTAL

A. Sensor fabrication and experimental setup

The planar Hall effect sensors used in this study rely on the anisotropy magnetoresistance of permalloy. The sensor stack consisting of Ta(3 nm)/$Ni_{80}Fe_{20}$(30 nm)/$Mn_{80}Ir_{20}$ (20 nm)/Ta(3 nm) was deposited with an easy direction along the *x*-direction as described by Østerberg *et al.*[22] The stack was patterned in the Wheatstone bridge geometries shown in Fig. 2, where N denotes the number of magnetoresistive segments in each sensor branch. Sensors with $N = 1$, 2, and 3 were fabricated. The sensors with $N = 3$ consist of an extra cell in each branch like the ones marked with dashed lines in Fig. 2. Each magnetoresistive segment has a length of $l = 250\,\mu$m and width of $w = 25\,\mu$m. A stack of Ti(5 nm)/Au(100 nm)/Pt(100 nm)/Ti(5 nm) is used for electrical contact and, on top, a 1 μm thick layer of Ormocomp was spin-coated to provide a pin-hole free protective layer.

In order to allow for electrical contact to the sensor, a click-on fluidic system[15,22] was used, which also defined the fluidic channel with dimensions length × width × height = 5 mm × 1 mm × 0.1 mm. The channel is defined such that the bottom branches of the dPHEB design are placed outside the channel. Thus, no magnetic beads affect these branches and $\beta_{\text{bottom}} = \gamma_{1,\text{bottom}} = 0$. The temperature of the sensors was kept constant at 25.0(1) °C using Peltier elements controlled by a LFI-3751 temperature controller (Wavelength Electronics, Inc., MT, USA). The setup was neither electrically nor magnetically shielded.

B. Measurements

In this section, a description of the measurement procedure and data treatment for the experimental studies on the three sensor designs is given. The focus of the study is on two different sets of experiments. First, to measure the sensor responses of the different sensor designs due to an externally applied magnetic field without magnetic beads present. Second, to measure the sensor signals vs. frequency of the different sensor designs due to the self-field with magnetic beads present.

1. External field dependence

To characterize the external field dependence of the three sensor designs, an alternating bias current with amplitude $I_{\text{AC}} = 1$ mA and frequency $f = 67$ Hz was passed through the sensors by a 6221 AC and DC Current Source (Keithley Instruments, USA), while measuring the 1st harmonic signal using a SR830 lock-in amplifier (Stanford Research Systems, USA) as function of the applied magnetic field in the *y*-direction. The applied magnetic field was generated by a custom made Helmholtz coil and swept from $\mu_0 H_y = -11$ mT to $\mu_0 H_y = 11$ mT and back. The field dependence of the 2nd harmonic signal was measured in the same manner, albeit with an AC bias current amplitude of $I_{\text{AC}} = 20$ mA.

2. Magnetic bead measurements

To characterize the dependence of the sensor signals on the presence of magnetic beads, measurements of the 2nd harmonic sensor signal vs. frequency were performed for the three sensor designs. These experiments were performed by first performing reference measurements with Milli-Q water in the fluidic channel. Then, a 1 mg/ml suspension of plain 80 nm Bionized NanoFerrite (BNF) starch beads (Micromod, Germany) was injected into the fluidic channel at a flow rate of 13.3 μl/min for 1.5 min and left stagnant for ~30 min before being flushed away with Milli-Q water.

The frequency sweeps of the sensor signal were performed by biasing the sensors with a current amplitude of $I_{\text{AC}} = 20$ mA supplied by a 6221 AC and DC Current Source and changing the frequency from 10.9 kHz to 1.9 Hz in 25 logarithmically equidistant steps. The 2nd harmonic sensor response was measured using a SR830 lock-in amplifier. Between points measured at various frequencies, reference points were recorded at 482 Hz to facilitate monitoring of the time dependence of the signal. A frequency sweep was recorded in 127 s.

3. Analysis of frequency sweeps

From the measurements of the 2nd harmonic sensor signal, it is possible to extract information about the hydrodynamic size of the bead suspension due to Brownian rotational diffusion (Brownian relaxation) of the magnetic beads.[8,23] The Brownian relaxation frequency f_{B} is given by

$$f_{\text{B}} = \frac{k_{\text{B}}T}{6\pi\eta V_{\text{h}}}, \tag{18}$$

where η is the viscosity of the liquid in which the beads are suspended, V_{h} is the hydrodynamic volume of the beads, and $k_{\text{B}}T$ is the thermal energy.

The beads are assumed to be spheres with diameters following the lognormal distribution:

$$f_{\text{LN}}(D_{\text{h}}) = \frac{1}{D_{\text{h}}\sigma\sqrt{2\pi}}\exp\left[-\frac{(\ln D_{\text{h}} - \mu)^2}{2\sigma^2}\right], \tag{19}$$

where μ is the logarithm to the median hydrodynamic diameter D_{hm}, $D_{\text{hm}} = \exp(\mu)$, and σ is the logarithmic standard deviation. The size distribution function is defined to be volume-weighted, i.e., the volume fraction of the particles with hydrodynamic diameters between D_{h} and $D_{\text{h}} + \text{d}D_{\text{h}}$ is $f_{\text{LN}}(D_{\text{h}})\text{d}D_{\text{h}}$. Thus, the distribution function takes into account that the sensor signal is proportional to the bead volume.

The fitting function used to analyze the 2nd harmonic sensor signal is given by[23]

$$\begin{aligned} V_{\text{fit}} &= V_2' + \text{i}V_2'' \\ &= \text{i}\int_0^\infty \frac{V_0 - V_\infty}{1 + \text{i}f/f_{\text{B}}(D_{\text{h}})} f_{\text{LN}}(D_{\text{h}})\text{d}D_{\text{h}} + \text{i}V_\infty \end{aligned} \tag{20}$$

with $V_0 = -2^{-3} I_{\text{AC}}^2 S_0 \gamma_1 \chi_0$ and $V_\infty = -2^{-3} I_{\text{AC}}^2 S_0 \gamma_1 \chi_\infty$, where χ_0 and χ_∞ are the DC and high frequency magnetic susceptibilities of the beads. In addition to V_0 and V_∞, the free fitting parameters are the median hydrodynamic diameter D_{hm} and the logarithmic standard deviation σ.

IV. RESULTS

A 3×3 mm^2 reference sample of the magnetic stack on the wafer was characterized by vibrating sample magnetometry and from the easy axis hysteresis loop, we obtained $\mu_0 H_{ex} = 3.30$ mT and $\mu_0 H_K = 0.50$ mT. From electrical measurements on a transmission line structure, we obtained $\rho_{av}/t = (\frac{1}{3}\rho_{\parallel} + \frac{2}{3}\rho_{\perp})/t = 8.49\ \Omega$ and $\Delta\rho/t = 0.16\ \Omega$ corresponding to an effective AMR ratio of 1.9% for the stack.

A. External field sensitivity

Figure 3 shows the 1st harmonic in-phase signal (panel (a)) and the 2nd harmonic out-of-phase signal (panel (b)) as function of applied external field for the three different sensor types with $N = 1$. In Fig. 3(a), the signals from the pPHEB to dPHEB sensors are multiplied by 100 to be observable on the same scale as for the PHEB sensor. In Fig. 3(b), the signal from the dPHEB sensor is multiplied by 50 to be observable on the same scale as the data for the PHEB and pPHEB sensors.

For the PHEB design, the 1st harmonic in-phase signal (Fig. 3(a)) depends linearly on the external field in the range $-2\,\text{mT} < \mu_0 H_y < 2\,\text{mT}$. No significant hysteresis or offset of the signal is observed. The corresponding 2nd harmonic out-of-phase signal is symmetric in the magnetic field with a value of about 40 μV in zero applied field. This value decays to zero for large applied magnetic fields.

For the pPHEB design, the 1st harmonic in-phase signal changes only slightly as function of applied field and the signal variation is about 500 times smaller than that observed for the PHEB sensor. However, the 2nd harmonic out-of-phase signal changes significantly with the applied magnetic field. It reaches a maximum value of about 51 μV for $\mu_0 H_y = 1$ mT and, like the PHEB sensor, it has a signal of about 40 μV in zero applied magnetic field.

For the dPHEB design, the 1st harmonic in-phase signal shows a linear region near $\mu_0 H_y = 0$ mT, but the slope is about 50 times smaller than that obtained for the PHEB sensor. The 2nd harmonic out-of-phase signal shows an approximately symmetric response with a magnitude, which is about 50 times smaller than that observed for the PHEB sensor.

Measurements corresponding to those presented in Fig. 3 were also recorded for all three sensor designs with $N = 2$ and $N = 3$ and showed similar behavior except that all signals were multiplied by factors of 2 and 3, respectively. The low-field sensitivities of the 1st harmonic in-phase signal for the PHEB sensors were found to $NS_0/\mu_0 = -181$ V/(TA), -369 V/(TA), and -555 V/(TA) for $N = 1$, 2, and 3, respectively.

B. Magnetic bead detection

Figure 4 shows the in-phase (top) and out-of-phase (bottom) 2nd harmonic sensor signal normalized with N vs. frequency for all three sensor designs with $N = 1$, 2, and 3. The

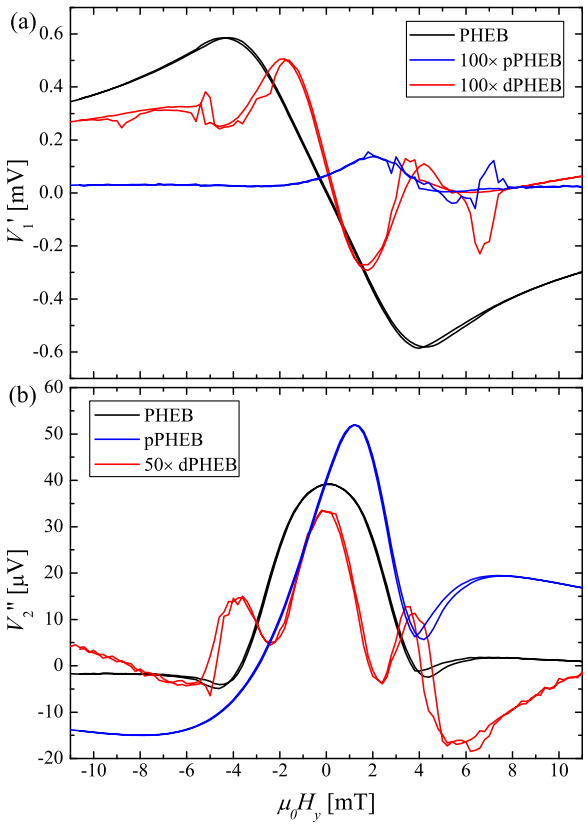

FIG. 3. (a) 1st harmonic in-phase ($I_{AC} = 1$ mA) and (b) 2nd harmonic out-of-phase ($I_{AC} = 20$ mA) sensor signals vs. magnetic field applied in the y-direction for the three different sensor types with $N = 1$. Note that some of the signals have been multiplied by factors of 50 or 100.

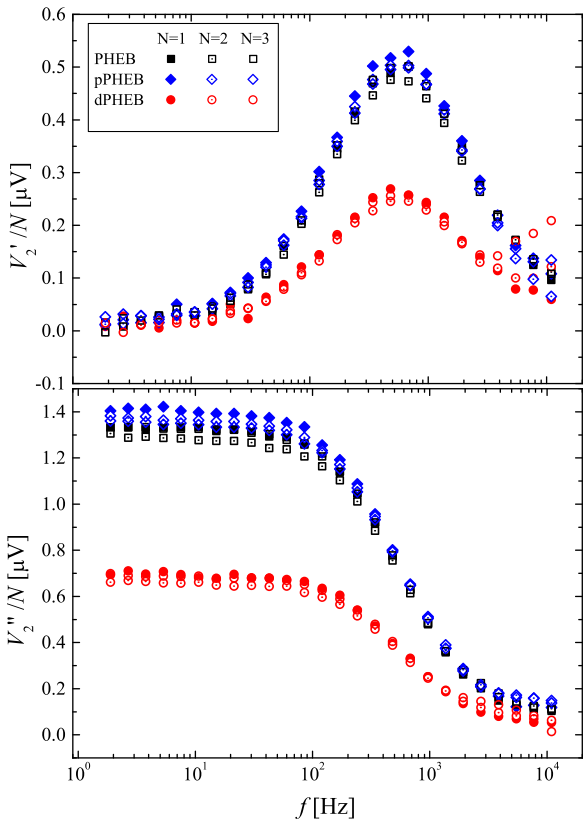

FIG. 4. In-phase (top) and out-of-phase (bottom) 2nd harmonic sensor signals normalized with N measured on a 1 mg/ml suspension of 80 nm magnetic beads vs. frequency for the three different sensor geometries with $N = 1$, 2, and 3. The signal level measured in the absence of magnetic beads was subtracted from all spectra.

data were measured ~30 min after injection of the magnetic bead suspension. The signal level prior to injection of the bead suspension was subtracted from the data. It is observed that the amplitudes are proportional to N and that the dPHEB design yields half the signal of the corresponding PHEB and pPHEB designs. It is also seen that, except for a few points at high frequencies, all nine spectra have the same shape. Thus, the sensor type and N only influence the amplitude of the signal, when the background has been subtracted. Table II reports the parameters obtained from fits of Eq. (20) to the data. Table II shows that the median hydrodynamic diameters found from least squares fits are around 94 nm and that the uncertainties are largest for the dPHEB design. The lognormal standard deviations are also found to agree well for all nine sensors with values around 0.25. The values of the scaling parameters V_0–V_∞ and V_∞ agree well with the ratios of the amplitudes observed from Fig. 4.

V. DISCUSSION

From the results presented in Sec. IV, it is clear that both signals due to external fields and magnetic beads are proportional to N. Thus, it is only necessary to discuss the behavior for the three different designs for a single value of N.

A. External field sensitivity

The linear theory presented in Sec. II, which is valid for low magnetic fields, predicts that the 1st harmonic in-phase sensor signal depends linearly on the applied magnetic field for the PHEB design, whereas zero signal with no field dependence is predicted for the pPHEB and dPHEB designs. This is validated by the results shown in Fig. 3(a), which show that the PHEB design indeed has a linear low-field response up to field values of about 2 mT. It is also seen that the signals from the pPHEB and dPHEB designs are reduced by factors of about 500 and 100 compared to that from the PHEB design, respectively. Furthermore, the remaining response of the dPHEB sensor is observed to be similar to that of the PHEB design. This likely originates from a small imbalance of the dPHEB design or from a small field inhomogeneity. Thus, the responses to an external magnetic field of the three investigated sensor designs agree well with the predictions.

For the 2nd harmonic out-of-phase signal, the linear theory presented in Sec. II predicts that the PHEB and pPHEB designs show the same low-field response with a constant non-zero signal level, whereas the dPHEB design is predicted to give zero signal. The measurements in Fig. 3(b) show that the V_2'' response of the PHEB design exhibits a flat symmetric peak centered at $\mu_0 H_y = 0$ mT with a peak value of about 40 μV. When the magnetic field increases, the signal drops towards zero. This observation agrees with the expected behavior—when the field increases beyond the linear low-field region, the sensor sensitivity decreases resulting in a reduced signal. As the sensor has a symmetric geometry, the effect of positive and negative magnetic fields is the same. Thus, a small applied magnetic field will not perturb the measured 2nd harmonic response for the PHEB design.

The pPHEB design shows the same signal as the PHEB design in zero applied magnetic field but displays an asymmetric response to an applied magnetic field. We attribute this behavior to the lower symmetry of the sensor geometry, which results in poor cancellation of higher order effects of the external magnetic field, combined with the sensor self-field and shape anisotropy of the sensor elements. The finite slope of the sensor response near $\mu_0 H_y = 0$ mT implies that the offset of V_2'' for the pPHEB design will be field sensitive even for small external magnetic fields.

The dPHEB design shows a symmetric response with respect to the applied magnetic field with a flat peak near $\mu_0 H_y = 0$ mT. The value of the peak is reduced by a factor of about 50 compared to that for the PHEB and pPHEB designs. This implies that the design efficiently reduces the sensor self-biasing by this factor and that this design is least influenced by external magnetic fields.

TABLE II. Parameters obtained from least squares fitting of Eq. (20) to the frequency sweeps of the 2nd harmonic sensor signal for the three different sensor designs. In the table, D_{hm} is the median hydrodynamic particle diameter and σ is the lognormal standard deviation. The remaining parameters refer to Eq. (20). The numbers in parentheses are 95% confidence intervals obtained from the least squares fitting. Only the data points in the range 1.9 Hz–2.7 kHz were used for the fits.

Type	N	D_{hm} [nm]	σ	V_0–V_∞ [μV]	V_∞ [μV]
PHEB	1	93.2(3)	0.26(1)	1.23(1)	0.1(1)
	2	93.9(3)	0.25(1)	2.33(1)	0.2(1)
	3	93.9(2)	0.25(1)	3.68(2)	0.3(1)
pPHEB	1	94.6(3)	0.26(1)	1.30(1)	0.1(1)
	2	94.7(2)	0.25(1)	2.47(1)	0.2(1)
	3	94.0(4)	0.26(1)	3.71(3)	0.3(1)
dPHEB	1	94.8(7)	0.24(2)	0.64(1)	0.1(1)
	2	93.9(3)	0.25(1)	1.21(1)	0.1(1)
	3	94.9(5)	0.24(1)	1.87(2)	0.2(1)

B. Magnetic bead detection

The presented results show that N can be increased to at least 3 to amplify the signal for the three different sensor designs. The total length of a sensor segment is limited by the maximum potential difference that can be applied across the sensor bridge without compromising the sensor operation in a liquid. The results also show that all sensor designs can be used for extracting the hydrodynamic size from frequency sweeps of the 2nd harmonic sensor signal and that the extracted hydrodynamic diameters are identical within the experimental uncertainty.

The signals due to magnetic beads for the PHEB and pPHEB designs were shown to be identical in agreement with the theoretical predictions. The pPHEB sensor has the advantage of being more compact than the PHEB design. This allows for a denser array of sensors inside the channel. Moreover, as the different sensor branches are placed closer together, effects of temperature and magnetic field inhomogeneities are reduced. Compared to the PHEB design, the 2nd harmonic sensor signal is easier to measure for the

pPHEB design because the 1st harmonic sensor signal is nominally zero. Due to the lack of mirror symmetry of the pPHEB design, the offset of the out-of-phase 2nd harmonic sensor signal has a stronger field-dependence compared to the PHEB design. However, only the in-phase 2nd harmonic sensor signal (corresponding to the out-of-phase magnetic susceptibility data) is needed for the analysis and hence this is not problematic.

The dPHEB design only gives half the signal from magnetic beads compared to the PHEB and pPHEB designs because only half of the sensor bridge is exposed to the magnetic beads. Moreover, this design reduces the sensor self-biasing offset by a factor of 50. Thus, for applications requiring measurements of small signal variations in the out-of-phase 2nd harmonic sensor signal, this design has a significant advantage over the PHEB and pPHEB designs. Such applications include the detection of surface-bound magnetic beads in the out-of-phase 2nd harmonic sensor signal at a fixed low frequency.[21] For frequency sweeps extending up to high frequencies on magnetic bead suspensions, the lack of a constant signal offset makes it difficult to use the sensor signal in the absence of magnetic beads to correct for instrumental phase shifts and these, therefore, have to be corrected for via measurements on, e.g., a paramagnetic salt. Since the points measured at high frequencies were omitted from the fits, the extracted hydrodynamic diameters correspond well with those obtained with the PHEB and pPHEB, except for slightly larger uncertainties.

C. Consequences for applications

Each sensor design has its pros and cons and, thus, the different designs are suited for different applications.

The symmetric PHEB design can be used both for detection of external magnetic fields as well as magnetic fields due to the sensor bias current. The sensitivity to external magnetic fields enables calibration of the low-field sensitivity to magnetic fields. As the sensor output signal is sensitive to both external magnetic fields and the magnetic bead signal, magnetic bead detection using the self-field should, for this design, be carried out in near-zero magnetic field conditions. The design can be considered to be general purpose applicable and required for basic sensor characterization.

The asymmetric pPHEB design has a sensitivity to external magnetic fields, which is about two orders of magnitude lower than that of the PHEB design at low magnetic fields, while maintaining the same signal due to magnetic beads magnetized by the self-field. Thus, this design is better suited for measurements at magnetic field conditions that deviate from near-zero, where a large 1st harmonic sensor signal due to an external magnetic field may interfere with measurements of the 2nd harmonic signal due to magnetic beads. However, due to the lower sensor symmetry, the out-of-phase 2nd harmonic signal offset due to sensor self-biasing has a stronger dependence on the external field. If needed, this offset and hence its variation can be reduced by modifying the magnetic stack. The sensor design is more compact than the PHEB design, which enables a denser sensor packing and potentially reduces the impact of gradients of temperature and the external magnetic field. Thus, the pPHEB design is well suited for measurements of the in-phase dynamic sensor signals under ambient conditions, e.g., for the characterization of the out-of-phase magnetic susceptibility of magnetic bead suspensions.

The symmetric and differential dPHEB design eliminates the sensitivity to external magnetic fields as well as the effect of the sensor self-biasing, but it only gives rise to half the magnetic bead signal compared to the other two designs. As the design has nominally zero offset in the 2nd harmonic signals, it is the best design for measurements of weak magnetic bead signals. For example, the amount of magnetic beads tethered to the sensor surface by a bioassay can be quantified in the in-phase magnetic susceptibility at low frequencies.[21] For measurements up to high frequencies, the lack of a sensor offset results in a more involved calibration procedure for correction for instrumental phase shifts.

We have shown for all designs that the signal increases proportional to N. In the present study, the measurement noise is dominated by the noise of the detection electronics and hence an increase of the sensor output results in an improved signal-to-noise. Thus, sensors with $N>1$ are expected to provide data with lower noise. From Table II, it is observed that the improved signal has no significant impact on the uncertainty on the determined hydrodynamic sizes and thus it may seem that there is no positive effect of increasing N. The cause of this may be that the hydrodynamic size is influenced by other physical parameters, such as if the liquid moves during a measurement. However, an improved signal-to-noise ratio enables measurements on magnetic bead suspensions with lower concentrations. A lower magnetic bead concentration enhances the sensitivity to interaction of a given number of beads with a sample and this may enhance the sensitivity of the bioassay. Moreover, a larger sensor area results in sampling of a larger sample volume, which may also improve the statistical sampling of the measurement. This effect is particularly important for larger magnetic bead sizes. A theoretical and experimental optimization of the bioassay sensitivity is a topic for our future work.

In this work, we have obtained a low-field sensitivity S_0 (cf. Eq. (5)), which normalized with the bar aspect ratio l/w assumes a value of $(S_0 w)/(l\mu_0) = -18.4\,\mathrm{V/(TA)}$. This value depends on the sensor stack. Hung *et al.* introduced the tri-layer stack Ta(3)/NiFe(10)/Cu(0.12)/IrMn(10)/Ta(3) (thicknesses in nm) for which they obtained a magnetic field sensitivity corresponding to $(S_0 w)/(l\mu_0) = -120\,\mathrm{V/(TA)}$,[24] which is about 6.5 times higher than that obtained in the present study. The scaling of the sensor signal with the sensor geometry for the detection of external magnetic fields has been demonstrated previously.[19,25,26] However, the present study is the first showing designs optimized for the detection of magnetic beads magnetized by the sensor self-field. In addition to the low-field sensitivity, the maximum allowed sensor bias current plays an important role as the self-field signal is proportional to the current squared. The optimization of the sensor stack and geometry to maximize the sensor self-field signal additionally depends on the sensor self-heating as well as a possible breakdown of the sensor coating and is a topic of our ongoing investigation.

VI. CONCLUSION

In conclusion, a systematic theoretical analysis of the construction of Wheatstone bridge magnetic sensors from basic sensor construction elements has been presented. Three different designs have been fabricated to determine experimentally the influence of an external magnetic field as well as the magnetic fields due to the sensor bias current. It has been shown that sensors can be designed to be nominally only sensitive to one of these magnetic field contributions. Furthermore, a method has been presented to scale up the sensor signal by appropriate combinations of multiple sensor segments. Specifically, two new scalable sensor designs have been presented, termed pPHEB and dPHEB, which are aimed towards the detection of magnetic beads magnetized by the sensor self-field and that are nominally insensitive to external magnetic fields. The pPHEB design uses an asymmetric bridge geometry, whereas the dPHEB design is a symmetric differential bridge design. For comparison, measurements were performed on a previously presented symmetric bridge design, termed PHEB, which is sensitive to both external magnetic fields and magnetic fields due to the sensor bias current.

This work shows an experimental investigation of the response of the three sensor designs and their upscaled versions to external magnetic fields as well as their response to magnetic fields due to the sensor bias current and it has been found that the results in the low-field regime agree well with the theoretical predictions. Moreover, the applicability is demonstrated of the three designs on measurements of the dynamic magnetic response of a magnetic bead suspension. The pros and cons of the three designs for magnetic bead detection have been discussed. The present work shows that the optimum sensor design depends strongly on the sensor application and the given sensor operating conditions. The results show that the pPHEB design efficiently cancels the signal due to low external magnetic fields and also provides a more compact sensor design. Hence, this design is suited for measurements of the Brownian relaxation dynamics on magnetic bead suspensions under ambient conditions. The dPHEB design, however, is found to be the best choice for surface-based bioassays.

The optimization of the magnetic stack and the sensor geometry to maximize the signal from magnetic beads magnetized by the sensor self-field is topic of our ongoing work.

ACKNOWLEDGMENTS

This work was supported by the Copenhagen Graduate School for Nanoscience and Nanotechnology (C:O:N:T) and the Knut and Alice Wallenberg (KAW) Foundation.

[1]I. Koh and L. Josephson, Sensors **9**, 8130 (2009).
[2]S. X. Wang and G. Li, IEEE Trans. Magn. **44**, 1687 (2008).
[3]N. Jaffrezic-Renault, C. Martelet, Y. Chevolot, and J.-P. Cloarec, Sensors **7**, 589 (2007).
[4]J. Göransson, T. Z. G. de la Torre, M. Strömberg, C. Russell, P. Svedlindh, M. Strømme, and M. Nilsson, Anal. Chem. **82**, 9138 (2010).
[5]J. Schotter, P. Kamp, A. Becker, A. Pühler, G. Reiss, and H. Brückl, Biosens. Bioelectron. **19**, 1149 (2004).
[6]P. P. Freitas, R. Ferreira, S. Cardoso, and F. Cardoso, J. Phys: Condens. Matter **19**, 165221 (2007).
[7]R. S. Gaster, D. A. Hall, C. H. Nielsen, S. J. Osterfeld, H. Yu, K. E. Mach, R. J. Wilson, B. Murmann, J. C. Liao, S. S. Gambhir, and S. X. Wang, Nat. Med. **15**, 1327 (2009).
[8]J. Connolly and T. G. S. Pierre, J. Magn. Magn. Mater. **225**, 156 (2001).
[9]H. Grossman, W. Myers, V. Vreeland, R. Bruehl, M. Alper, C. Bertozzi, and J. Clarke, Proc. Natl. Acad. Sci. U.S.A. **101**, 129 (2004).
[10]A. P. Astalan, F. Ahrentorp, C. Johansson, K. Larsson, and A. Krozer, Biosens. Bioelectron. **19**, 945 (2004).
[11]F. Ludwig, S. Mäuselein, E. Heim, and M. Schilling, Rev. Sci. Instrum. **76**, 106102 (2005).
[12]A. Ranzoni, J. Schleipen, L. van IJzendoorn, and M. Prins, Nano Lett. **11**, 2017 (2011).
[13]D. R. Baselt, G. U. Lee, M. Natesan, S. W. Metzger, P. E. Sheehan, and R. J. Colton, Biosens. Bioelectron. **13**, 731 (1998).
[14]B. T. Dalslet, C. D. Damsgaard, M. Donolato, M. Strømme, M. Strömberg, P. Svedlindh, and M. F. Hansen, Lab Chip **11**, 296 (2011).
[15]F. W. Østerberg, B. T. Dalslet, D. Snakenborg, C. Johansson, and M. F. Hansen, AIP Conf. Proc. **1311**, 176–183 (2010).
[16]B. D. Boer, J. Kahlman, T. Jansen, H. Duric, and J. Veen, Biosens. Bioelectron. **22**, 2366 (2007).
[17]C. Hong, C. Wu, Y. Chiu, S. Yang, H. Horng, and H. Yang, Appl. Phys. Lett. **88**, 212512 (2006).
[18]P. I. Nikitin, P. M. Vetoshko, and T. I. Ksenevich, J. Magn. Magn. Mater. **311**, 445 (2007).
[19]A. D. Henriksen, B. T. Dalslet, D. H. Skieller, K. H. Lee, F. Okkels, and M. F. Hansen, Appl. Phys. Lett. **97**, 013507 (2010).
[20]T. B. G. Hansen, C. D. Damsgaard, B. T. Dalslet, and M. F. Hansen, J. Appl. Phys. **107**, 124511 (2010).
[21]G. Rizzi, F. Østerberg, M. Dufva, and M. Hansen, Biosens. Bioelectron. **52**, 445 (2014).
[22]F. W. Østerberg, G. Rizzi, T. Z. G. de la Torre, M. Strömberg, M. Strømme, P. Svedlindh, and M. F. Hansen, Biosens. Bioelectron. **40**, 147 (2013).
[23]F. W. Østerberg, G. Rizzi, and M. F. Hansen, J. Appl. Phys. **113**, 234508 (2013).
[24]T. Q. Hung, S. Oh, B. Sinha, J.-R. Jeong, D.-Y. Kim, and C. Kim, J. Appl. Phys. **107**, 09E715 (2010).
[25]S. Oh, P. Patil, T. Q. Hung, B. Lim, M. Takahashi, D. Y. Kim, and C. Kim, Solid State Commun. **151**, 1248 (2011).
[26]F. W. Østerberg, A. D. Henriksen, G. Rizzi, and M. F. Hansen, J. Appl. Phys. **114**, 106101 (2013).